Proton Storage in Metallic $H_{1.75}MoO_3$ Nanobelts through Grotthuss Mechanism

Wangwang Xu[1,7,‡], Kangning Zhao[2,3,‡,*], Xiaobin Liao[3,‡], Congli Sun[3], Kun He[4], Yifei Yuan[4,5], Wenhao Ren[6], Jiantao Li[5], Tianyi Li[7], Chao Yang[8], Hongwei Cheng[2,*], Qiangchao Sun[2], Ingo Manke[8], Xionggang Lu[2], Jun Lu[5,*]

1. College of Materials and Chemical Engineering, Hubei Provincial Collaborative Innovation Center for New Energy Microgrid, Key Laboratory of Inorganic Nonmetallic Crystalline and Energy Conversion Materials, China Three Gorges University, Yichang 443002, P. R. China

2. State Key Laboratory of Advanced Special Steel & Shanghai Key Laboratory of Advanced Ferrometallurgy & School of Materials Science and Engineering, Shanghai University, Shanghai 200444, P. R. China

3. State Key Laboratory of Advanced Technology for Materials Synthesis and Processing, International School of Materials Science and Engineering, Wuhan University of Technology, Wuhan 430070, P. R. China

4. College of Chemistry and Materials Engineering, Wenzhou University, Wenzhou 325035, P. R. China

5. Chemical Sciences and Engineering Division, Argonne National Laboratory, Lemont, Illinois 60439, United States

6. Institute of Chemical Sciences and Engineering, École Polytechnique Fédérale de Lausanne (EPFL), ISIC-LSCI, Lausanne 1015, Switzerland

7. Advanced Photon Sources, Argonne National Laboratory, Lemont, Illinois 60439, USA

8. Helmholtz Centre Berlin for Materials and Energy, Hahn-Meitner-Platz 1, Berlin 14109, Germany

KEYWORDS: Proton-ion battery; non-metal charge carrier; Metallic; MoO_3; Grotthuss mechanism.

ABSTRACT: Proton, as the cationic form of the lightest element-H, is regarded as most ideal charge carrier in "rocking chair" batteries. However, current researches on proton batteries are still at the infancy and they usually deliver low capacity and suffer from severe acidic corrosion. Herein, electrochemically activated metallic $H_{1.75}MoO_3$ nanobelts are developed as a stable electrode for proton storage. The electrochemically pre-intercalated protons not only bond directly with the terminal O3 site *via* strong O-H bonds, but also interact with the oxygens within the adjacent layers through hydrogen bonding, forming a hydrogen-bonding network in $H_{1.75}MoO_3$ nanobelts and enabling a diffusion-free Grotthuss Mechanism as a result of its ultralow activation energy of ~0.02 eV. To the best of our knowledge, this is the first reported inorganic electrode exhibiting Grotthuss mechanism-based proton storage. Additionally, the proton intercalation into MoO_3 with formation of $H_{1.75}MoO_3$ induces strong Jahn-Teller electron-phonon coupling, rendering metallic state. As a consequence, the $H_{1.75}MoO_3$ shows an outstanding fast charging performance and maintaining a capacity of 111 mAh/g at 2500 C, largely outperforming the state-of-art battery electrodes. More importantly, symmetric proton ion full cell based on $H_{1.75}MoO_3$ was assembled and delivered an energy density of 14.7 Wh/kg at ultrahigh power density of 12.7 kW/kg, which ouperforms those of fast charging supercapacitors and lead-acid batteries.

Introduction

An ideal energy storage device would store a large amount of energy with light weight and in short time.[1] Based on the caculaiton of therotical capacity of electrode, the lower the atomic mass of charge carriers, the larger the theoretical energy density can be delivered.[2] Lithium ion batteries (LIBs) have occupied the most of consumer market share of portable energy storage devices in regards to the low atomic weight of Li.[3] However, owning to the limited resources and rising price of Li as well as the low rate capability, it is very challenging to expand LIBs to grids-level energy storage.[4] Therefore, large number of research efforts have been spent on the batteries utilizing earth-abundent elements as charge carriers.[5] However, non-metal ions are ignored, especially proton ions, which is more plentiful on earth compared to the metallic charge carriers.[6] Moreover, as ideal charge carriers, proton ions have the unique features of very small radius (a single proton), and fast diffusion via the proton hopping/Grotthuss mechanism, enabling superfast intercalation and deintercalation in aqueous batteries.[7] However, electrodes for proton ion battery are still largely unexplored and the assocaited reaction mechanisms are neither intensively understood.

Efforts have been spent on developing novel electrode material for proton battery in aqueous and non-aqueous electrolyte[8]. Previous researches focusing on organic electrode, including 3,4,9,10-perylenetetracarboxylic dianhydride[9] and poly(3,4-ethylenedioxythiophene)[10], as well as inorganic electrode such as $WO_3 \cdot 0.6H_2O$[11], MoO_3[12], Turnbull's blue[7a], have reported good cyclability of these electrode materials. However, previous studies suggest that MoO_3 undergoes rather sluggish diffusion-controlled behaviour of H^+ storage in MoO_3[13]. Thus, boosting the kinetic of the electrode would be crucial in achieving high power application in MoO_3. Expanding the interlayer gap of MoO_3 using H_2O molecules is suggested to be an efficient stragety to boost the charge-storage kinetics of electrodes[14] and is usually achievable in aqueous battery by solvated ion intercalation[15]. On the other hand,

recent studies revealed that solids with abundunt hydrogen-bonding networks would take the advantages of Grotthuss conduction, such as hydrated metal–organic frameworks[16] or even for lithium conduction[17]. Recently, our group have successfully demonstrated Prussian blue analogue for fast proton conduction enabled by the continuous hydrogen-bonding network inside the lattice [7a]. Grotthuss proton conduction is widely accepted as reason for the for the ultra fast proton conduction, and would boost the charge transfer kinetics by orders of magnitude[7a]. However, currently there are no reports verifying the Grotthuss mechansim in inorganic materials.

Herein, we target the electrochemically activated metallic $H_{1.75}MoO_3$ nanobelts as electrode for proton ion battery, which takes the advantages of Grotthuss proton conduction as verified by the ultralow activation energy measured both experimentally and therotically. $H_{1.75}MoO_3$ nanobelts maintain a high capacity of 111 mAh/g at the current density of 2500 C (1C = 200 mA/g) for 5000 cycles, outperforming the state-of-art proton insertion electrodes, wiping out the hoping mechansim and confirming the Grotthuss proton conduction mechanism in metallic $H_{1.75}MoO_3$ nanobelts. The full cell based on symetric $H_{1.75}MoO_3$ nanobelts delivered an energy density of 14.7 Wh/kg at a maxim power density of 12.7 kW/kg, demonstrating its potential suitability for grid-scale high-power energy storage device. Addtionally, proton intercalation into MoO_3 host induces strong Jahn-Teller electron-phonon coupling, rendering the metallic electrode upon activation.

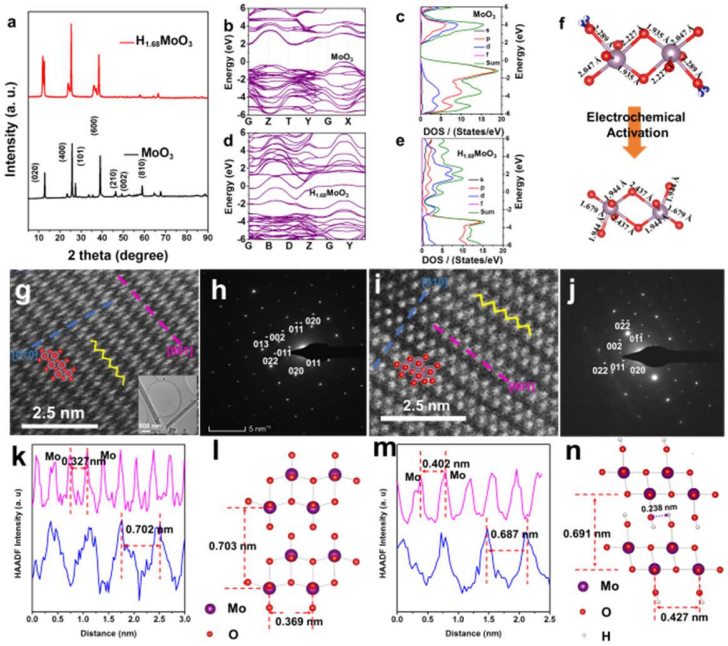

Figure 1. (a) XRD of MoO_3 and $H_{1.75}MoO_3$ nanobelts. (b, d) Band structure and (c, e) electronic density of state of α-MoO_3 and $H_{1.75}MoO_3$, respectively. All the energy valus are in reference to the femi level. (f) Schemetic illutration of the transition of MoO_3 to $H_{1.75}MoO_3$ through Jahn-Teller effect. (g) high-resolution HAADF STEM image, and (h) the SAED pattern of MoO_3 nanobelts under zoon axis of [100]. (k) The intensity line scan along the layer and vertial to the layer in Figure 1g. (l) MoO_3 crystal viewed along the [001] direction. (i) High-resolution HAADF STEM image and j) the corresponding SAED pattern of $H_{1.75}MoO_3$ nanobelts. (m) The intensity line scan along the layer and vertial to the layer in Figure 1i. (n) $H_{1.75}MoO_3$ crystal viewed along the [001] direction.

Discussion

Pure phase α-MoO_3 are prepared *via* one-step hydrothermal method with well defined nanobelts morphology as confirmed in Figure S1 and act as precursor for the electrochemical activation. The synthesis procedure is described in detail in supporting information. During the initial discharging process (Figure S2), MoO_3 nanobelts transform to $H_{1.75}MoO_3$ nanobelts with the intercalation of protons. The structural change and electronic properties during the electrochemical activation process are carefully studied *via* X-ray diffraction (XRD), scanning transmission electron microscope (STEM), and density functional theory (DFT) calculation. XRD patterns of MoO_3 nanobelts in Figure 1a show diffraction peaks at 12.69°, 23.28°, 25.57°, 27.45°, 38.97°, 46.17°, and 58.99°, which correspond to the (020), (101), (400), (210), (600), (002), and (810) planes of orthorhombic MoO_3 (JCPDF card no. 04-008-4311). After discharging to -0.4 V to realize electrochemical avtivation, the obtained $H_{1.75}MoO_3$ nanobelts maintain the orthorhombic structure with the entire proton intercalation. XRD patterns in Figure 1a reveal that the (020) peak at 12.80° moves towards lower angle (to 12.35°) with the interlayer spacing expanding from 6.9 Å to 7.2 Å (Figure S2a), which is also confirmed by synchrotron XRD in Figure S2b. The expanded interlamellar spacing is primarily due to the improved interactions between the layers with the intercalated protons[18]. Atomic-level study of the electrochemical activation process was conducted by high angle annular dark field (HAADF) STEM images and SAED patterns in Figure 1. The HAADF images shown in Figure 1g and 1i reveal the zigzag array of Mo atoms in both MoO_3 and $H_{1.75}MoO_3$ nanobelts propagates preferentially along the [001] direction. The apparent Van der Waals gap between the zigzag arrays of Mo atoms reveal the layered structure of both pristine MoO_3 and $H_{1.75}MoO_3$ crystals. From the selected area (electron) diffraction (SAED) patterns in Figure 1h and 1j, $H_{1.75}MoO_3$ nanobelts still maintain the orthorhombic symmetry, while atomic distance between Mo atoms along different directions was carefully studied in HAADF STEM images. Figure 1e shows the intensity line scan along the layer and vertial to the layer in Figure 1g, showing the atomic distance between Mo atoms along [010] and [001] dirctions, respectively as illustrated in Figure 1f.

The d-spacings along [010] and [001] dirctions are 0.69 and 0.33 nm on average, respectively, which are in consistent with the schematic structure of α-MoO_3 viewed from [100] direction (Figure 1i). After electrochemical activation, as shown in Figure 1i and 1j, the d-spacings along [010] and [001] dirctions are 0.73 and 0.41 nm on average, respectively, suggesting the structural distortion induced by the proton intercalation. The intercalated protons are bonded with terminal oxygens (the apical O atoms pointing to the Van der Waals gaps) of MoO_6 octahedrons, resulting in the elongated Mo-O bonds and expanded (001) planes. Moreover, the reaction mechanism is also investigated by *in-situ* Raman spectra. As shown in Figure S3 and S4, upon initial discharge process, the graduate disappearance of sharp peak at 989.6 cm^{-1} indicates the breaking of asymmetric Mo-O3 stretching vibrations at terminal sites of MoO_6 octahedrons and the formation of O3-H bonds with intercalated proton[19]. Moreover, in Figure 1k-n, the bonding length between proton and the terminal oxygens in the adjacent layers is about 0.238 nm, suggesting the existence of hydrogen bonds in $H_{1.75}MoO_3$ lattice.

The band structures of MoO_3 and $H_{1.75}MoO_3$ are studied by DFT calculations in Figure 1b-1e and Figure S5. The MoO_3 shows a band gap of 1.9 eV while no band gap is observed in $H_{1.75}MoO_3$, suggesting the metallic nature of the $H_{1.75}MoO_3$ in Figure 1b. To further elucidate the origin of the metallic state of $H_{1.75}MoO_3$, we further projected density of states (DOS) onto the oxide slab. As is known, three types of oxygen environment exist in MoO_3, namely the asymmetric bridging O1, the symmetric bridging O2, and the terminal O3. After proton intercalation, the interaction of O3 p orbitals with intercalated proton ions leads to a positive shift of Mo d orbital. Consequently, the valence band at maximum of S and the conduction minimum at X shift towards lower energy values. After proton intercalation, Mo layers relax alternately towards rows of bridging oxygen, O1 and O2, breaking the glide-plane symmetry. In this way, the Jahn-Teller distortion leads to a semimetal-to-metal transition.[20]

To evaluate the proton storage properties of $H_{1.75}MoO_3$ nanobelts, three-electrode cells based on $H_{1.75}MoO_3$ nanobelts are assembled and tested in a voltage window of -0.38 to 0.7 V. Figure S6 represents the Cyclic Voltammetry (CV) curves in the initial cycle. Electrochemical activation takes place during the initial discharging process, leading to the formation of $H_{1.75}MoO_3$ nanobelts. The CV at initial cycle shows the broad cathodic peaks at 0.058, -0.12, and -0.31 V due to the insertion of protons and while the CV curves in subsequent two cycles in Figure 2a show two pairs of redox peaks at 0.23/-0.019 V and -0.22/-0.33 V are observed. The different CV curves confirm the activation process of MoO_3 in acidic electrolyte. Figure 2b summarizes the stability test of $H_{1.75}MoO_3$ nanobelts at 100 A/g for 50 cycles and the $H_{1.75}MoO_3$ nanobelts deliver the high initial specific capacity of 188 mAh/g and maintain a capcity of 153 mAh/g after 50 cycles, with capacity retention of ~81 %. The rate performances are summarized in Figure 2c from 50 to 700 A/g. At 50 A/g, the $H_{1.75}MoO_3$ nanobelts maintain a capacity of 233 mAh/g with two obvious platform which correpsonds well the CV curves in Figure 2a, and notably, at 600 A/g, $H_{1.75}MoO_3$ nanobelts retain a high discharge capacity of 115 mAh/g. The large voltage drop is related to the internal resistance when the ultrahigh current passes through the battery. We also compare our rate performance with the state-of-art proton ion battery in Figure 2d and the $H_{1.75}MoO_3$ nanobelts retains not only the highest capacity at rather low current density, but also the largest rate up to 700 A/g, within a charging time less than 1 s. Moreover, to test the long cycle stability, the cells are tested at 500 A/g for over 5000 cycles. In Figure 2e, $H_{1.75}MoO_3$ nanobelts deliver an initial specific charge capacity of 111 mAh/g and after 5000 cycles, $H_{1.75}MoO_3$ nanobelts maintain the capacity of 89 mAh/g, corresponding to a capacity retention of 80%, indicating remarkable long cycling stability. The capacity decay is believed to be related to the gradual etching of the electrode in the acidic electrolyte (Figure S7).

The electrochemical kinetics of proton intercalation into $H_{1.75}MoO_3$ electrode were studied by analytical approaches to quantitatively distinguish the diffusion or capacitive controlled proton storage processes. Notably, CV curves maintain similar shapes, despite the increasing scan rates in Figure 3a. The anodic/cathodic peaks are still obvious at 120 mV/s. Power-law relationship is applied[12e, 21] to describe the kinetics as below:

$$i = av^b \quad (1)$$

and log(*i*) *vs.* log(*v*) follows the linear relationships and b-value can be solved at each peak in Figure 3b. The *b* value is determined by the slope, and calculated to be 0.92, 0.84, 0.80, and 0.79 (Figure 3c), respectively, implying that the current response of $H_{1.75}MoO_3$ nanobelts is domniated by capacitive behavior. The equation is further expanded in the full voltage window as below:

$$i = k_1 v + k_2 v^{1/2} \quad (2)$$

Based on the caculation, the results show that with the rising of the scan rate, the contribution ratio of capacitive is increased to 98.8% at 100 mV/s, revealing the dominance effect of capacitive behavior at high rate. Additionally, a pair of new redox peaks at 0.43/0.27 V is observed, which is belived to to be related to new intercalation site in $H_{1.75}MoO_3$ nanobelts.

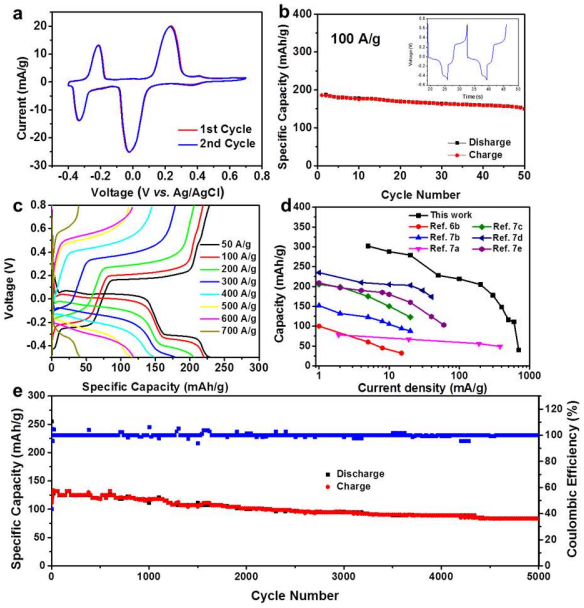

Figure 2. (a) CV curves at 10 mV/s in the initial two cycles. (b) Cycling performance at 50 A/g with charge/discharge profile inset. (c) Rate performance at ultrahigh current density up to 700 A/g and (d) comparison of the state-of-art proton insertion battery electrode. (e) Long term cycling stablity test at 500 A/g.

Furthermore, to investigate the electrochemical kinetics of $H_{1.75}MoO_3$ nanobelts-based proton battery, the Electrochemical Impedance Spectroscopy (EIS) of the cell at different states are implemented. In Figure S8, the spectrum is composed of a compressed semi-circle at high frequency implying the charge-transfer resistance in the electrode and in both charged and

discharged states show very low charge-transfer resistance, which is is endowed by the metallic state electrode. The Arrhenius plot based temperature-dependent charge transfer resistance in Figure 3d and Figure S9 reveals the ultralow activation energy of 0.02 eV, which suggest a desolvation free charge transfer process in the electrode/electrolyte interface, confirming the fast migration of hydronium ions. Furthermore, the ultralow activation energy derived from proton transport of 0.23 eV also verifies the Grotthuss mechanism-dominated proton conduction in $H_{1.75}MoO_3$. To provide better mechanistic insight in the diffusion of proton into the proton-defiecient $H_{0.19}MoO_3$ and proton-rich $H_{1.75}MoO_3$ structures, we performed DFT caculation to consider the proton insertion into proton-defiecient state $H_{0.19}MoO_3$ host structure. The proton transport mechanism involves a transition state where proton is bonded to two neighboring O ions. The activation energy dervied from the DFT caculation is only 0.14 eV (Figure 3e), which suggests that proton diffusion in proton-defiecient $H_{0.19}MoO_3$ requires minum energy and is close to that of Grotthuss mechanism. Moreover, when one proton is removed from its own structure, the proton in proton-rich $H_{1.75}MoO_3$ structure would, after relaxation, migrates to next O3 site as displayed in Figure 3g. which further confirms the spontaneous proton transport and further verifies the Grotthuss mechanism. To further verify this, we also computed different proton number in H_xMoO_3 structure, spontaneous proton transport is observed until the proton number is 1.1 in the structure in Figure 3f. Taken together, the ultralow activation energy derived from the experimental and caculation results suggest the direct relationship of the Grotthuss mechanism in either proton-rich $H_{1.75}MoO_3$ nanobelts or proton-deficient $H_{0.19}MoO_3$.

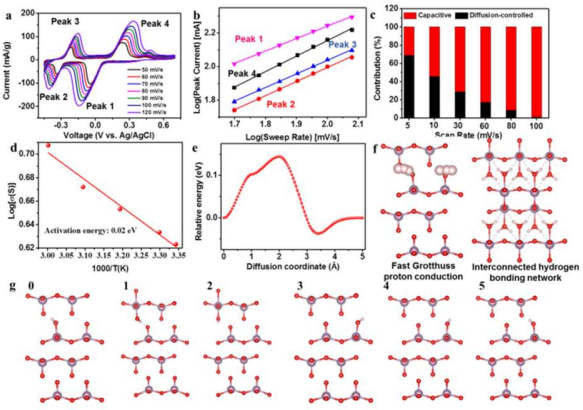

Figure 3. (a) CV curves at different scan rates ranging from 5 to 100 mV/s, (b) Randles-Sevcik plot obtained from the CV data, (c) the contribution ratio of the capacitive and diffusion-limited capacities at different scan rates, (d) plots of logS against 1000/T for $H_{1.75}MoO_3$ nanobelts. (e) The diffusion energy battier and (f, g) the diffusion paths in proton-rich $H_{1.75}MoO_3$ nanobelts and proton-defiecient $H_{0.19}MoO_3$.

The *ex-situ* XRD patterns were performed at typical depth of discharge states during the first cycles. As displayed in Figure 4b, during discharge process, the peak at 12.35° slightly decreases to a higher angle of 11.72° from state I to Ⅳ, with the interlayer space expanding from 7.2 Å to 7.5 Å. The increased interlamellar spacing is ascribed to the extraction of protons during the charging process. When the electrode is discharged to -0.38 V, the characteristic peak at 11.7° returns back to a lower angle at 12.38°, revealing reversible structural change. To investigate the valence state change of the electrode material, *ex-situ* XPS was carried out at different states. The pristine MoO_3 nanobelts in Figure S10 is composed of two band energies at 232.9 and 236.1 eV, which can be ascribed to 3d5/2 and 3d3/2 peaks of Mo^{6+}, repectively. Compared with pristine MoO_3, at the initial state of $H_{1.75}MoO_3$ nanobelts, Mo 3d spectrum in Figure 4c and d displays two more bands located at 231.7 and 234.9 eV, which are the characteristic peaks of Mo^{5+}, indicating that the valance of Mo is reduced with the intercalation of protons. As shown in Figure 4d, upon charging, the two big bands located at 231.7 and 234.9 eV still exist, indicating that Mo^{5+} is partially oxidized to Mo^{6+}. This phenomenon suggests that a portion of protons are extracted from $H_{1.75}MoO_3$ during the charging process. The O 1s XPS spectra in Figure 4e and 4f further confirm the redox reaction during activation and charging process. In Figure S10b, the dominant O 1s peak located at 530.8 eV is ascribed to molybdenum trioxide in pristine MoO_3 nanobelts. After the electrochemical activation, the O 1s peak was deconvoluted and two new peaks at 531.3 and 532.6 eV represent Mo pentoxide and oxygen bonded with protons, respectively. At charging state, the area of O 1s peak at 532.6 eV decreases and the area of O 1s peak at 532.6 eV increases, indicating Mo is partially oxidized back to Mo^{6+}, and protons partially break the bonding with oxygen. These results reveal that only a portion of protons in $H_{1.75}MoO_3$ nanobelts can be reversibly extracted. To identify the intercalation sites and confirm the structural reversibility of $H_{1.75}MoO_3$ upon extraction and insertion of protons, *in-situ* Raman spectroscopy was conducted. Figure 4g-i display the *in-situ* Raman spectrum of $H_{1.75}MoO_3$ nanobelts and its charge and discharge curves during *in-situ* Raman testing. As shown in Figure 4h, the characteristic peak intensity of initial $H_{1.75}MoO_3$ is low. Upon charge to 0.5 V, it presents significantly increased intensities of all the peaks. When discharged to -0.38 V, the intensities of all the peaks become weaker again. The weakening of the Raman may be related to the decreased crystalinity as evidenced by the *ex-situ* XRD in Figure 4a. In five cycles, Raman spectroscopy present periodically increase and decrease in peak intensity along with charging and discharging reversibly and this phenomenon indicates that the structure of bilayered $H_{1.75}MoO_3$ shows increased symmetric degree with the extraction of protons. Upon discharging, decreased intensity reflects asymmetry, introduced with the inserted protons. The increase and decrease on intensity of Raman spectrum upon charge and discharge reveal the high reversibility of structural change with the insertion and extraction of protons. Detailed change of *in-situ* Raman spectrum can be observed with normalized intensity. As displayed in Figure 4i, at the initial state, $H_{1.75}MoO_3$ nanobelts show two peaks located at 300.4 and 737.1 cm^{-1}. The broad peak at 300.4 cm^{-1} is assigned to the wagging modes of the terminal Mo=O groups while the sharp peak at 737.1 cm^{-1} corresponds to the symmetric Mo-O-Mo stretching.[22] When the cell is charged to 0.5 V, two new sharp peaks appeared at 973.5 and 1053.2 cm^{-1}. The strong new peak at 973.5 cm^{-1} can be assigned to the asymmetric Mo=O stretching.[22-23] Additionally, the small peak at 1053.2 cm^{-1} can be assigned to the singly coordinated oxygen with molybdenum, which is sensitive to the oxidization state of Mo.[21] The appearance of these two peaks indicates the debonding of protons with terminal oxygens and the formation of Mo=O at the terminal sites of MoO_6 octahedrons. Meanwhile, the Mo^{5+} is oxidized to Mo^{6+}. After discharging to -0.38 V, these two new peaks gradually disappear, suggesting the breaking of Mo-O3 bonds and the regeneration of O-H bonds. This evidence validates that the terminal oxygens are the active sites for protons conduction. The structural change upon intercalation of protons is highly reversible, with the formation of hydrogen-bonding network in MoO_3 structure.

The STEM-HAADF experiments were further acquired from the $H_{1.75}MoO_3$ phase after full charge. As shown in Figure 4j, after charged to 0.5 V, $H_{1.75}MoO_3$ still maintains the orthorhombic symmetry. The zigzag array of Mo atoms still propagates

preferentially along the [001] direction, indicating no phase transformation with the extraction of protons. To investigate the structural change, atomic distance between Mo atoms is further measured. Figure 4k shows the intensity line scan along the layer and vertial to the layer in Figure 4j. Compared with the atomic distance in $H_{1.68}MoO_3$, the sample shows increased atomic distances along [010] and [001] dirctions, which are about 0.711 and 0.378 nm, respectively. The increased atomic distance probally results from the breaking of Mo-O-H bond and the generation of the shortened Mo=O bonds, leading to the expanded lattice along both (010) planes and (001) planes. Therefore, w the electrochemical reactions is described as shown in Figure 4l. During the electrochemical activation, the initial discharge process on the cathode side is:

$$MoO_3 + 1.75\ H^+ + 2.10\ e^- \rightarrow H_{1.75}MoO_3 \quad (3)$$

and in the subsequent cycles, the redox reaction for peak 1/4 is:

$$H_{1.75}MoO_3 \leftrightarrow H_{0.74}MoO_3 + 1.01\ H^+ + 1.01\ e^- \quad (4)$$

the redox reaction for peak 2/3 is:

$$H_{0.74}MoO_3 \leftrightarrow H_{0.19}MoO_3 + 0.55\ H^+ + 0.55\ e^- \quad (5)$$

Furthermore, the micron-sized MoO_3 is also ultilized for testing the electrochemical proton storage performance and shows indentical redox behavior, but with slightly lower capacity at high current, which is suspected to be linked with the less active sites (Figure S11).

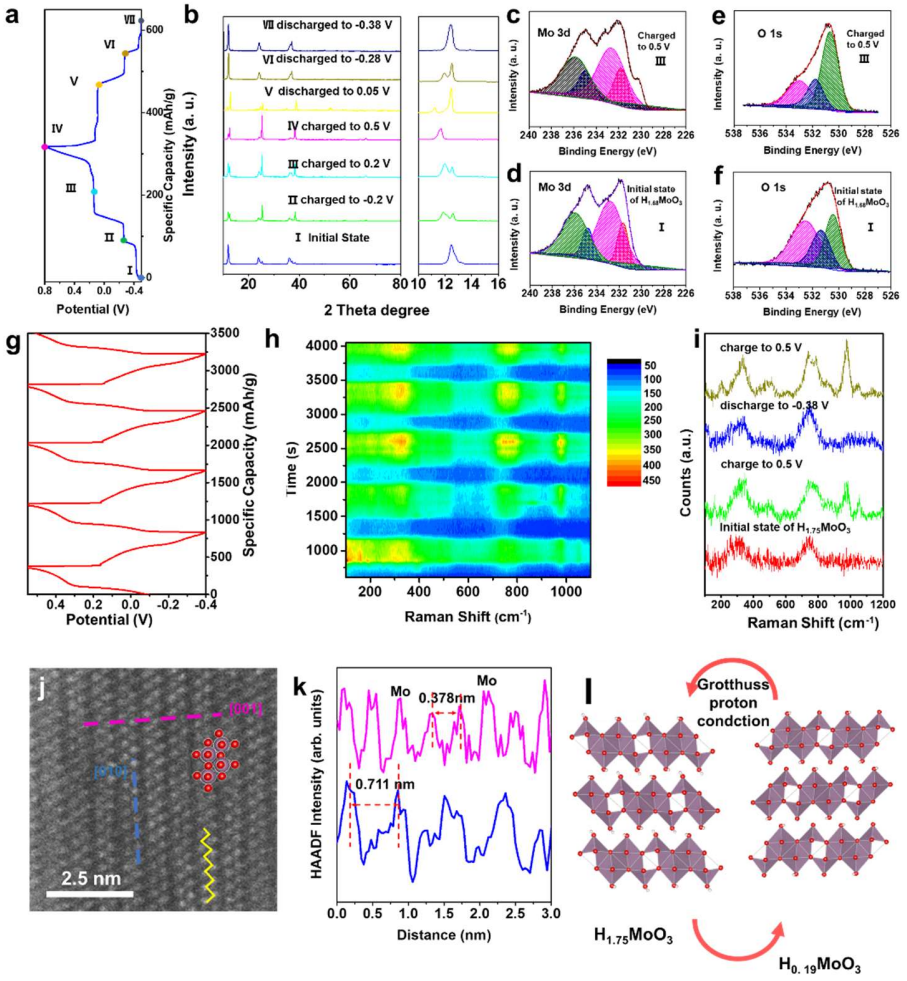

Figure 4. (a) Typical charge and discharge curves under the current density of 5 A/g, (b) *ex-situ* XRD patterns of $H_{1.75}MoO_3$ nanobelts collected at selected voltages, XPS spectra of Mo 3d at (c) initial and (d) charge states, and O 1s at I initial and (f) charge states. (g) Charge and discharge curves for the *in-situ* Raman testing, (h) *in-situ* Raman spectra of $H_{1.75}MoO_3$ nanobelts collected during the five cycles shown in Figure 4g and (i) the Raman spectrum with normalized intensity at different states. (j) High-resolution HAADF STEM image of $H_{1.75}MoO_3$ after fully charged, (k) intensity line scan along the layer and vertial to the layer in the HAADF image, (l) schemetic illutration of protons deintercalation and intercalation in $H_{1.75}MoO_3$ during following reversible cycles.

Based on the two distict peaks from MoO_3, the symetrical proton ion full cell made of two MoO_3 electrodes ultilizes redox reactions (4) at high voltage as cathode and redox reactions (5) at low voltage as anode as shown in Figure 5a. The stability test in Figure 5b reveals the long-term cyclability at 20 A/g for over 1000 cycles. The electrochemical working window is from -0.70 to 1.35 V *vs.* Ag/AgCl. All redox reaction of the symetrial MoO_3 electrode are involved in the electrochemical working window and thus no

side reactions such as hydrogen/oxygen evolution reaction are involved in the full cell. Initially, the cycling performance at 20 A/g is tested and the full cell retains 75% of the initial capacity after 1000 cycles. The rate performance of the full cell is further investigated from 20 to 100 A/g in Figure 5c and the charge-discahrge curves in Figure 5d shows stable voltage output at ~ 0.4 V, which is consensus with the CV curves and remarkably, the full cell delivers an outstanding rate capability with 138 and 120 mAh/g (caculated by the mass of cathode material) at 20 and 100 A/g, respectively. Minor capacity loss is observed at ultrahigh current, further confirming fast Grotthuss proton transporting mechanism in metallic $H_{1.75}MoO_3$. More importantly, the maxim power density can reach as high as 12.7 kW/kg at energy density of 14.7 Wh/kg while the maxium energy density of 59 Wh/kg at power density of 8.7 kW/kg, demonstrating the potential for high power, grid scale energy storage device.

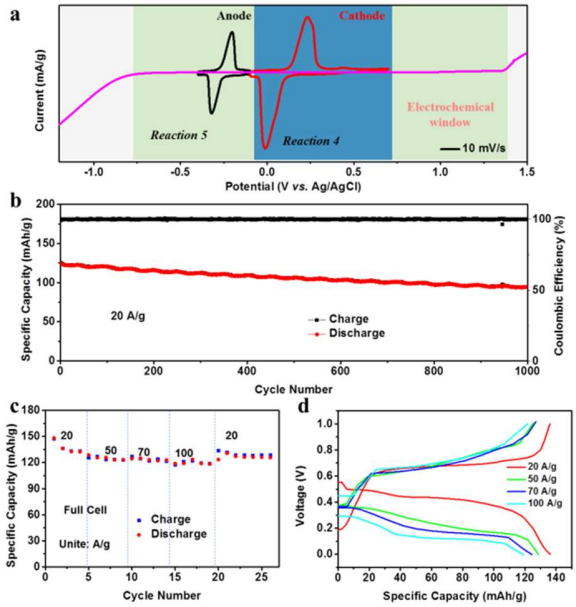

Figure 5. (a) CV curves of MoO_3-based symetrical proton ion full cell. (b) Cycling performance at 20 A/g. (c, d) Rate performance and the charge-discharge curves of the full cell.

Conclusions

In summary, we first report the Grotthuss mechanism-driven ultrafast proton storage in inorganic electrode materials *via* a facile electrochemical activation/protonation process transforming MoO_3 to metallic $H_{1.75}MoO_3$. The loosenly packed O3 in the edge of the layer of metallic $H_{1.75}MoO_3$ acts as proton binding site for fast Grotthuss proton conduction as evidenced by the ultralow activation energy of ~0.02 eV. The metallic $H_{1.75}MoO_3$ shows a excellent rate capability as well as high capcity as proton insertion electrode. At high current density of 500 A/g, $H_{1.75}MoO_3$ nanobelts is able to maintain reversible capacity of 111 mAh/g for over 5000 cycles within charging time of less than 1 second, largely outperforming the state-of-the-art proton batteries. Furthermore, a symmetric proton full cell based on two $H_{1.75}MoO_3$ electrodes delivered the energy density of 14.7 Wh/kg at maxim power density of 12.7 kW/kg, which ouperforms those of supercapacitor and lead-acid battery, demonstrating its promising applicable future for high power, grid scale energy storage device. Our report on the ultrafast proton storage electrode through Grotthuss mechanism would boost the study on battery systems with non-metal ions as charge carriers.

ASSOCIATED CONTENT

This material is available free of charge via the Internet at http://pubs.acs.org.

- Detailed materials, experimental procedures, characterization methods, computational methods, supporting figures including characterizations of MoO_3, detailed explanation of activation energy of charge transfer resistance and proton conductivity, and ex-situ characterizations of $H_{1.75}MoO_3$ nanobelts tables.

AUTHOR INFORMATION

Corresponding Author

* Kangning Zhao - State Key Laboratory of Advanced Special Steel & Shanghai Key Laboratory of Advanced Ferrometallurgy & School of Materials Science and Engineering, Shanghai University, Shanghai 200444, P. R. China. Email: *vicyel@shu.edu.cn*; *vicyel@126.com*.

* Hongwei Cheng - State Key Laboratory of Advanced Special Steel & Shanghai Key Laboratory of Advanced Ferrometallurgy & School of Materials Science and Engineering, Shanghai University, Shanghai 200444, P. R. China. Email: *hwcheng@shu.edu.cn*

*Jun Lu - Chemical Sciences and Engineering Division, Argonne National Laboratory, Lemont, Illinois 60439, United States. Email: *junlu@anl.gov*

Author Contributions

W.X., K.Z., and X.L. contributed equally.

Notes

The authors declare no competing financial interest.

ACKNOWLEDGMENT

The authors acknowledge the financial support from the National Natural Science Foundation of China (21905169, 21905305, and 51874196) and the Shanghai Pujiang Program (2019PJD015), the Iron and Steel Joint Research Fund of National Natural Science Foundation and China Baowu Steel Group Corp. Ltd (U1860203), and the Program for Professor of Special Appointment at the Shanghai Institutions of Higher Learning (TP2020032). Work at Argonne National Laboratory was supported by the U. S. Department of Energy (DOE), Office of Energy Efficiency and Renewable Energy, Vehicle Technologies Office. Argonne National Laboratory is operated for DOE Office of Science by UChicago Argonne, LLC, under contract number DE-AC02-06CH11357.

REFERENCES

1. (a) Mai, L.; Yan, M.; Zhao, Y., Track batteries degrading in real time. Nature News 2017, 546 (7659), 469; (b) Shin, W.; Lu, J.; Ji, X., ZnS coating of cathode facilitates lean‐electrolyte Li‐S batteries. Carbon Energy 2019, 1 (2), 165-172.

2. Liu, Z.; Li, H.; Zhu, M.; Huang, Y.; Tang, Z.; Pei, Z.; Wang, Z.; Shi, Z.; Liu, J.; Huang, Y., Towards wearable electronic devices: A quasi-solid-state aqueous lithium-ion battery with outstanding stability, flexibility, safety and breathability. Nano Energy 2018, 44, 164-173.

3. (a) Zuo, X.; Zhu, J.; Müller-Buschbaum, P.; Cheng, Y.-J., Silicon based lithium-ion battery anodes: A chronicle perspective review. Nano Energy 2017, 31, 113-143; (b) Zhao, K.; Zhang, L.; Xia, R.; Dong, Y.; Xu, W.; Niu, C.; He, L.; Yan, M.; Qu, L.; Mai, L., SnO_2 Quantum Dots@Graphene Oxide as a High-Rate and Long-Life Anode Material for Lithium-Ion Batteries. Small 2016, 12 (5), 588-594; (c) Sun, C.; Liao, X.; Xia, F.; Zhao, Y.; Zhang, L.; Mu, S.; Shi, S.; Li, Y.;

Peng, H.; Tendeloo, G. V., High Voltage Cycling Induced Thermal Vulnerability in $LiCoO_2$ Cathode: Cation Loss and Oxygen Release Driven by Oxygen Vacancy Migration. ACS nano 2020; (d) Yu, Z.; Wang, B.; Liao, X.; Zhao, K.; Yang, Z.; Xia, F.; Sun, C.; Wang, Z.; Fan, C.; Zhang, J., Boosting Polysulfide Redox Kinetics by Graphene‐Supported Ni Nanoparticles with Carbon Coating. Advanced Energy Materials 2020, 2000907.

4. Liu, K.; Liu, Y.; Lin, D.; Pei, A.; Cui, Y., Materials for lithium-ion battery safety. Science advances 2018, 4 (6), eaas9820.

5. (a) Xu, W.; Wang, Y., Recent progress on zinc-ion rechargeable batteries. Nano-Micro Letters 2019, 11 (1), 90; (b) Huang, J.; Guo, Z.; Ma, Y.; Bin, D.; Wang, Y.; Xia, Y., Recent progress of rechargeable batteries using mild aqueous electrolytes. Small Methods 2019, 3 (1), 1800272; (c) Yang, Q.; Wang, Y.; Li, X.; Li, H.; Wang, Z.; Tang, Z.; Ma, L.; Mo, F.; Zhi, C., Recent Progress of MXene-Based Nanomaterials in Flexible Energy Storage and Electronic Devices. Energy & Environmental Materials 2018, 1 (4), 183-195; (d) Zhao, K.; Wang, C.; Yu, Y.; Yan, M.; Wei, Q.; He, P.; Dong, Y.; Zhang, Z.; Wang, X.; Mai, L., Ultrathin Surface Coating Enables Stabilized Zinc Metal Anode. Advanced Materials Interfaces 2018, 5 (16); (e) Lian, S.; Sun, C.; Xu, W.; Huo, W.; Luo, Y.; Zhao, K.; Yao, G.; Xu, W.; Zhang, Y.; Li, Z., Built-in oriented electric field facilitating durable $ZnMnO_2$ battery. Nano energy 2019, 62, 79-84; (f) Yao, Y.; Yu, L.; Wang, M.; Dai, A.; Zhang, Y.; Guo, Q.; Lin, Y.; Wen, J.; Wu, F.; Ji, X., Burning magnesium in carbon dioxide for highly effective phosphate removal. Carbon Energy 2021, 3 (2), 330-337.

6. (a) Zhu, Y. h.; Yang, X.; Zhang, X. b., Hydronium ion batteries: a sustainable energy storage solution. Angewandte Chemie International Edition 2017, 56 (23), 6378-6380; (b) Liang, G.; Wang, Y.; Huang, Z.; Mo, F.; Li, X.; Yang, Q.; Wang, D.; Li, H.; Chen, S.; Zhi, C., Initiating Hexagonal MoO_3 for Superb-Stable and Fast NH_4^+ Storage Based on Hydrogen Bond Chemistry. Advanced Materials 2020, 32 (14), 1907802.

7. (a) Wu, X.; Hong, J. J.; Shin, W.; Ma, L.; Liu, T.; Bi, X.; Yuan, Y.; Qi, Y.; Surta, T. W.; Huang, W., Diffusion-free Grotthuss topochemistry for high-rate and long-life proton batteries. Nature Energy 2019, 4 (2), 123-130; (b) Wang, X.; Xie, Y.; Tang, K.; Wang, C.; Yan, C., Redox Chemistry of Molybdenum Trioxide for Ultrafast Hydrogen‐Ion Storage. Angewandte Chemie International Edition 2018, 57 (36), 11569-11573; (c) Tie, Z.; Liu, L.; Deng, S.; Zhao, D.; Niu, Z., Proton Insertion Chemistry of a Zinc–Organic Battery. Angewandte Chemie International Edition 2020, 59 (12), 4920-4924; (d) Su, Z.; Ren, W.; Guo, H.; Peng, X.; Chen, X.; Zhao, C., Ultrahigh Areal Capacity Hydrogen‐Ion Batteries with MoO_3 Loading Over 90 mg cm^{-2}. Advanced Functional Materials 2020, 2005477; (e) Yan, L.; Huang, J.; Guo, Z.; Dong, X.; Wang, Z.; Wang, Y., Solid-State Proton Battery Operated at Ultralow Temperature. ACS Energy Letters 2020, 5 (2), 685-691; (f) Park, M. J.; Yaghoobnejad Asl, H.; Manthiram, A., Multivalent-ion versus proton insertion into battery electrodes. ACS Energy Letters 2020, 5 (7), 2367-2375.

8. Xu, Y.; Wu, X.; Jiang, H.; Tang, L.; Koga, K. Y.; Fang, C.; Lu, J.; Ji, X., A Non‐aqueous Proton Electrolyte Enables Stable Cycling of Proton Electrodes. Angewandte Chemie.

9. Wang, X.; Bommier, C.; Jian, Z.; Li, Z.; Chandrabose, R. S.; Rodríguez‐Pérez, I. A.; Greaney, P. A.; Ji, X., Hydronium‐ion batteries with perylenetetracarboxylic dianhydride crystals as an electrode. Angewandte Chemie 2017, 129 (11), 2955-2959.

10. (a) Emanuelsson, R.; Sterby, M.; Strømme, M.; Sjödin, M., An all-organic proton battery. Journal of the American Chemical Society 2017, 139 (13), 4828-4834; (b) Yuan, Y.; Lu, J., Demanding energy from carbon. Carbon Energy 2019, 1 (1), 8-12.

11. Jiang, H.; Hong, J. J.; Wu, X.; Surta, T. W.; Qi, Y.; Dong, S.; Li, Z.; Leonard, D. P.; Holoubek, J. J.; Wong, J. C., Insights on the proton insertion mechanism in the electrode of hexagonal tungsten oxide hydrate. Journal of the American Chemical Society 2018, 140 (37), 11556-11559.

12. (a) Xu, W.; Sun, C.; Zhao, K.; Cheng, X.; Rawal, S.; Xu, Y.; Wang, Y., Defect engineering activating (Boosting) zinc storage capacity of MoS_2. Energy Storage Materials 2019, 16, 527-534; (b) Dong, Y.; Xu, X.; Li, S.; Han, C.; Zhao, K.; Zhang, L.; Niu, C.; Huang, Z.; Mai, L., Inhibiting effect of Na+ pre-intercalation in MoO_3 nanobelts with enhanced electrochemical performance. Nano energy 2015, 15, 145-152; (c) Zhao, Y.; Goncharova, L. V.; Lushington, A.; Sun, Q.; Yadegari, H.; Wang, B.; Xiao, W.; Li, R.; Sun, X., Superior Stable and Long Life Sodium Metal Anodes Achieved by Atomic Layer Deposition. Advanced Materials 2017, 29 (18), 1606663; (d) Haocheng, G.; Damian, G.; Neeraj, S.; Wenhao, R.; Zhen, S.; Aditya, R.; Chuan, Z., Two-Phase Electrochemical Proton Transport and Storage in α-MoO3 for Proton Batteries. Cell Reports Physical Science 2020, 1 (10), 100225; (e) Brezesinski, T.; Wang, J.; Tolbert, S. H.; Dunn, B., Ordered mesoporous α-MoO_3 with iso-oriented nanocrystalline walls for thin-film pseudocapacitors. Nature materials 2010, 9 (2), 146-151.

13. Liang, G.; Mo, F.; Ji, X.; Zhi, C., Non-metallic charge carriers for aqueous batteries. Nature Reviews Materials 2020, 1-15.

14. Yu, M.; Shao, H.; Wang, G.; Yang, F.; Liang, C.; Rozier, P.; Wang, C.-Z.; Lu, X.; Simon, P.; Feng, X., Interlayer gap widened α-phase molybdenum trioxide as high-rate anodes for dual-ion-intercalation energy storage devices. Nature communications 2020, 11 (1), 1-9.

15. Wang, N.; Sun, C.; Liao, X.; Yuan, Y.; Cheng, H.; Sun, Q.; Wang, B.; Pan, X.; Zhao, K.; Xu, Q., Reversible (De) Intercalation of Hydrated Zn^{2+} in Mg^{2+}-Stabilized V_2O_5 Nanobelts with High Areal Capacity. Advanced Energy Materials 2020, 10 (41), 2002293.

16. Wong, N. E.; Ramaswamy, P.; Lee, A. S.; Gelfand, B. S.; Bladek, K. J.; Taylor, J. M.; Spasyuk, D. M.; Shimizu, G. K., Tuning intrinsic and extrinsic proton conduction in metal–organic frameworks by the lanthanide contraction. Journal of the American Chemical Society 2017, 139 (41), 14676-14683.

17. Yuan, S.; Bao, J. L.; Wei, J.; Xia, Y.; Truhlar, D. G.; Wang, Y., A versatile single-ion electrolyte with a Grotthuss-like Li conduction mechanism for dendrite-free Li metal batteries. Energy & Environmental Science 2019, 12 (9), 2741-2750.

18. Johnson, J. W.; Jacobson, A. J.; Brody, J. F.; Rich, S. M., Coordination intercalation reactions of the layered compounds vanadyl phosphate ($VOPO_4$) and vanadyl arsenate ($VOAsO_4$) with pyridine. Inorganic Chemistry 1982, 21 (10), 3820-3825.

19. SrinivasaRao, K.; Kanth, B. R.; Mukhopadhyay, P., Optical and IR studies on rf magnetron sputtered ultra-thin MoO_3 films. Applied Physics A 2009, 96 (4), 985-990.

20. (a) Hamedi, M. M.; Hajian, A.; Fall, A. B.; Hakansson, K.; Salajkova, M.; Lundell, F.; Wagberg, L.; Berglund, L. A., Highly conducting, strong nanocomposites based on nanocellulose-assisted aqueous dispersions of single-wall carbon nanotubes. ACS nano 2014, 8 (3), 2467-2476; (b) Braïda, B.; Adams, S.; Canadell, E., Concerning the Structure of Hydrogen Molybdenum Bronze Phase III. A Combined Theoretical− Experimental Study. Chemistry of materials 2005, 17 (24), 5957-5969; (c) Whittingham, M. S., Hydrogen motion in oxides: from insulators to bronzes. Solid State Ionics 2004, 168 (3-4), 255-263; (d) Quek, S. Y.; Biener, M. M.; Biener, J.; Friend, C. M.; Kaxiras, E., Tuning electronic properties of novel metal oxide nanocrystals using interface interactions: MoO_3 monolayers on Au (1 1 1). Surface science 2005, 577 (2-3), L71-L77.

21. (a) Simon, P.; Gogotsi, Y.; Dunn, B., Where do batteries end and supercapacitors begin? Science 2014, 343 (6176), 1210-1211; (b) Augustyn, V.; Come, J.; Lowe, M. A.; Kim, J. W.; Taberna, P.-L.; Tolbert, S. H.; Abruña, H. D.; Simon, P.; Dunn, B., High-rate electrochemical energy storage through Li^+ intercalation pseudocapacitance. Nature materials 2013, 12 (6), 518-522.

22. Yan, B.; Zheng, Z.; Zhang, J.; Gong, H.; Shen, Z.; Huang, W.; Yu, T., Orientation controllable growth of MoO_3 nanoflakes: micro-Raman, field emission, and birefringence properties. The Journal of Physical Chemistry C 2009, 113 (47), 20259-20263.

23. Lee, S.-H.; Seong, M. J.; Tracy, C. E.; Mascarenhas, A.; Pitts, J. R.; Deb, S. K., Raman spectroscopic studies of electrochromic a-MoO_3 thin films. Solid State Ionics 2002, 147 (1-2), 129-133.

Insert Table of Contents artwork here